Satellite-Observed Warm-Core Structure in Relation to Tropical Cyclone Intensity Change

Xiang Wang[1,2*], Haiyan, Jiang[2] , Jun A. Zhang[3], and Ke Peng[1]

[1] Joint Centre for Data Assimilation Research and Application/Institute for Climate and Application Research/Institute for Climate and Application Research, Nanjing University of Information Science & Technology, Nanjing, China

[2] Department of Earth & Environment, Florida International University, Miami, Florida

[3] Cooperative Institute for Marine and Atmospheric Studies, University of Miami, and NOAA/AOML/Hurricane Research Division, Miami, Florida

Submitted to Atmospheric Research

Dec. 2nd, 2019; Revised on Feb.2, 2020

* Corresponding author at: School of Atmospheric Sciences, Nanjing University of Information Science & Technology, No. 219, Ningliu Road, Pukou District, Nanjing, China, 210044. Phone: +8615895930154.
E-mail: wangxiang@nuist.edu.cn.

Abstract

Using a 13-year dataset of Atmospheric Infrared Sounder (AIRS) retrieved temperature profiles including 5019 AIRS overpasses in 1061 tropical storm through category-2 tropical cyclones (TCs) in global basins during 2002-2014, this study examines the relationship between the warm-core structure and TC intensity change with a focus on rapid intensification (RI). The AIRS TC overpasses are classified into RI, slowly intensifying (SI), neutral (N), and weakening (W) categories. The effect of the warm-core structure upon TC intensification is entangled with that upon TC intensity. It is necessary to exclude the weakening category in order to single out the relationship between TC intensification and warm-core structure from a statistical method. The composite warm-core maximum temperature anomaly is the strongest in RI storms (~7 K), followed by W (~6 K), SI (~5 K) and N (~ 4K) storms. RI storms have the highest equivalent potential temperature (θ_e) and CAPE in the eye among all intensity change categories. The warm-core structure of RI storms is asymmetric relative to shear, with the higher temperature anomaly and convective available potential energy (CAPE) located in the down-shear quadrant. When only considering samples with intensification rates ≥ 0, a significant and positive correlation is found between the warm-core strength and TC intensification rate. The warm-core height is also positively correlated with the TC intensification rate at a high confidence level. The AIRS-derived warm-core temperature anomaly greater than 4 K and weighted warm-core height higher than 450 hPa are the necessary conditions for RI.

1. Introduction

The prediction of tropical cyclone (TC) intensity change, especially rapidly intensification (RI), has proven to be a challenging problem, although the intensity guidance of TCs has improved substantially over the last several decades (DeMaria et al., 2014) due to more accurate numerical models and more satellite observations over the open ocean. It is well accepted that RI is more likely to occur under favorable environmental conditions, including a warm ocean surface and mixed layer, low environmental vertical wind shear, and high relative humidity, conditional instability, large scale upper-level divergence, and low-level convergence, etc. (Merrill 1988; Kaplan & DeMaria, 2003; Wang & Wu, 2004; Kaplan et al., 2010). However, the false-alarm ratio of forecasting algorithms using only environmental predictors remains undesirably high, especially during slowly intensifying events (Kaplan et al. 2010; Shu et al. 2012). Hendricks et al. (2010) found that similarly favorable environmental conditions are often present in both RI and slowly intensifying cases, suggesting that environmental factors alone are not sufficient for accurate forecast of RI, and the internal dynamic and thermodynamic processes may play a more important role in RI.

Convective and precipitation processes within the inner core region of TCs are well recognized to be important for RI. Recent studies have found that hot towers occurring within the inner core region were related to the intensification of TCs (Hendricks et al., 2004; Kelley et al., 2004, 2005; Montgomery et al., 2006; Houze et al., 2009; Jiang, 2012). For example, using 6 years of the well-observed over flights of TCs by the TRMM precipitation radar, Kelley et al. (2004) argued that the chance of TC RI increased when one or more tall precipitation cells existed in the eyewall. Increased precipitation coverage has also been linked to RI using large satellite observational datasets. Cecil and Zipser (1999) found that TC intensity change in the 24-h future shown a positive correlation with the spatial coverage of at least moderate rain rates using 85-GHz brightness temperatures. Jiang (2012) found that several parameters relating to inner-core convection were more intense in RI storms than non-RI storms. It was further determined that RI requires a minimum threshold for inner-core raining area and volumetric rain that is appreciably higher than non-RI storms (Jiang & Ramirez, 2013).

More recently it has been demonstrated based on satellite observations that a high degree of axisymmetry of precipitation, convective, and thermodynamic parameters is associated with the subsequent RI (Kieper & Jiang 2012; Zagrodnik & Jiang 2014; Alvey et al. 2015; Tao & Jiang 2015; Zawislak et al. 2016; Tao et al. 2017; Xu et al. 2017; Shimada et al. 2017; Fischer et al. 2018; Jiang et al. 2018). This is consistent with idealized numerical modeling results that suggested that the TC vortex intensified as a symmetric response to the azimuthally averaged latent heat release within convection (Nolan & Grasso, 2003; Nolan et al., 2007).

Besides the abovementioned inner core convective and precipitation parameters, the warm-core structure has also been linked with the TC intensification (Stern & Zhang, 2013; Stern et al., 2015; Lin & Tian, 2019). Many numerical case studies have demonstrated that the development and evolution of warm-core strength and height are associated with subsequent RI. Zhang & Chen (2012) found that higher-level warm cores can induce greater drops in the sea level pressure than lower-level ones due to the more amplification effects of the higher-level warming based on the hydrostatic balance using a 72-h cloud-permitting numerical simulation of Hurricane Wilma (2005). Similar results were found by Hirschberg & Fritsch (1993) and Chen & Zhang (2013). Analyses upon the successful simulations also disclosed that the formation of the upper level warm core coincided with the onset of RI for Hurricane Wilma (2005, Zhang & Chen 2012). Kieu et al. (2014) argued that a middle-to-upper tropospheric temperature perturbation was a necessary constraint to the onset of TC RI in their idealized Hurricane Weather Research and Forecast (HWRF) model simulations. Through an idealized experiment of a TC in a radiative convective equilibrium with an SST of 31^{o}C, Ohno & Satoh (2015) found that the inner-core maximum temperature anomaly occurred at 9 km during most of the intensification period, while a secondary upper-level warm core only developed once the TC reached near-major hurricane strength. More recently, in their numerical simulations of Hurricane Edouard (2016), Munsell et al. (2018) found that at Edouard's peak intensity the maximum inner-core temperature anomaly occurred between 4 and 8 km. In addition, the evolution of the inner-core perturbation temperatures indicated that weak to moderate warming (~4 K) began to occur in the low to mid-levels 24-48 hours prior to RI, and this warming significantly strengthened and deepened 24 hours after RI has begun. They also argued that the height and amplitude of the maximum temperature anomaly is not a necessary condition for RI onset in the ensemble experiment. Therefore, based on these numerical studies, it is still an open question on whether and how the warm-core structure is associated with RI.

On the other hand, little research has been done statistically on the relationship between the TC warm-core structure and intensity change using observational approaches. The ability of satellite sounder-based temperature retrievals to resolve the TC warm-core structure has been questioned by Stern & Nolan (2012) due to the cold anomaly problem in below-10-km levels by Advanced Microwave Sounding Unit (AMSU) data as shown in Knaff et al. (2004). Nevertheless, to avoid the uncertainties of AMSU retrievals in the lower level, Lin and Qian (2019) examined the relationships between AMSU-based temperature anomaly in the upper troposphere and lower stratosphere and TC intensity and RI. They found that the upper-level warm core strength increases with TC intensity and hurricanes are associated with warm core above eyewall cloud top extending into the stratosphere. They also found that RI storms are associated with strong warming rate above eyewall cloud top extending into the stratosphere, indicating that stratospheric downdrafts might be involved in RI. Recently, using aircraft dropsonde-derived temperature profiles in hurricanes, Wang & Jiang (2019) evaluated the accuracy of temperature retrievals from combined Atmospheric Infrared Sounder (AIRS) and AMSU observations in TCs. They found that the AIRS+AMSU product can resolve the TC warm-core structure well, comparable to the dropsonde observations, although the AMSU-A alone retrievals fail to do so. They demonstrated that the bias of the AIRS+AMSU good and best quality retrievals relative to dropsonde data is within 1–2 K on average for multiple TCs during September 2014.

Using a 11-year database of AIRS+AMSU retrieved temperature profiles for TCs in the western north Pacific basin, Gao et al. (2017) found a negative correlation between the warm-core strength and 24-h intensity change, whereas no relationship was found between the warm-core height and intensity change. Gao et al.'s (2017) study was mainly focused on different warm-core structures for various TC intensities. Their results on the relationship between the warm-core structure and TC intensity are consistent with Wang & Jiang's (2019) results from AIRS data for global TCs. However, the negative correlation between the warm-core strength and 24-h intensity change found by Gao et al. (2017) is contradictory to modeling studies mentioned above which showed that a strengthened warming in the eye is associated with RI (Zhang & Chen 2012; Chen & Zhang 2013; Munsell et al. 2018). Therefore, this study will extend Gao et al.'s (2017) study into all global basins and seek to reconcile these contradictory results by re-investigating the relationship between the warm-core structure and TC intensity change. We will focus on the comparison of AIRS+AMSU-derived warm-core strength and height for four different TC intensity change categories including RI, slowly intensifying (SI), neutral (N), and weakening (W) using a 13-year global database of AIRS+AMSU-derived temperature profiles. Section 2 provides a description of the data and methods applied in this study. The warm core structures of TCs and their relationship with intensity change are presented in Section 3. Conclusions are summarized in Section 4.

2. Data and methodology

2.1. The AIRS+AMSU dataset

In May 2002, the Aqua satellite carrying the AIRS and AMSU as well as other sensors was successfully launched into sun-synchronous orbit from a 705-km altitude (Aumann et al. 2003; Chahine et al. 2006). The AIRS instrument is of 2378 infrared channels, capable of providing the atmospheric temperature retrievals with a vertical resolution of ~1 km. However, contaminations of infrared-based temperature retrievals due to cloud and rain must be corrected. The AIRS+AMSU (AIRS for short) level 2 product used an advanced cloud-clearing technique (Chahine et al. 2001; Susskind et al. 2003; Moustafa et al. 2006) that employs microwave observations from AMSU along with the AIRS observations to remove cloud contaminations and retrieve temperature and humidity profiles. This study uses the standard AIRS version 6 level 2 temperature and humidity products during August 2002 to December 2014 with a horizontal resolution of 45 km, same as in Wang & Jiang (2019). The AIRS overpasses are in about 1650-km swath width, and available twice daily. The AIRS dataset used in this study only contains the temperature retrievals with best or good quality at 12 pressure levels from 1000 to 100 hPa. Specifically, best-quality data individually meet the designed accuracy requirements (i.e., absolute accuracy of 1 K in 1-km thick layers in the troposphere) and good-quality data meet the accuracy requirements only when temporally and/or spatially averaged. For more details about the AIRS dataset and the verification of AIRS temperature retrieval against aircraft-deployed dropsonde data in TCs, please see Wang & Jiang (2019).

2.2. Selection of AIRS overpasses in TCs and classification of TC intensity change categories

Using the 6-hourly TC best-track data obtained from the National Hurricane Center (NHC) for northern Atlantic (ATL) and eastern and central Pacific (EPA) basins and from the Joint Typhoon Warning Center (JTWC) for northwestern Pacific (NWP), northern Indian Ocean (NIO), southern Indian Ocean (SIO), and South Pacific (SPA) basins, the TC maximum sustained wind intensity (V_{max}) and storm center location are linearly interpolated to match the observational time of AIRS. Since not all TCs can be well observed by the AIRS with its swath width of ~1650 km, here we only select the AIRS overpasses which can capture the TC center. In order to eliminate the impacts of TC intensity and other factors on the warm core strength that are not due to TC intensity change, especially RI, several criteria are applied to the selection of AIRS overpasses. By following Zagrodnik & Jiang (2014), the following criteria are applied: mean SST> 26 ℃, mean environmental vertical wind shear < 16 m s^{-1}, the storm center is within $\pm 30^o$ latitude, and the intensity of the storm at the time of the overpass is between tropical storm and category-2 hurricane. The AIRS level-2 standard products also provide total precipitable water (TPW), cloud fraction, and sea surface temperature (SST) retrievals. The mean SST, cloud fraction, and TPW are calculated by averaging all values within 500 km radius from the TC center for AIRS TC overpasses. The mean environmental vertical wind shear, averaged between 200–850 hPa and 500–750 km radius from the TC center (Zagrodnik & Jiang 2014), is derived from the European Centre for Medium-Range Weather Forecasts (ECMWF) interim (Dee et al. 2011) reanalysis data. In addition, only those overpasses with available temperature profiles with good or best quality at all levels between 1000 and 150 hPa are used in this study.

The final dataset consists of a total of 5019 AIRS TC overpasses from 1061 TCs in global basins between August 2002 to December 2014. We stratify the overpasses into four TC intensity change categories, including RI, slowly intensifying (SI), neutral (N), and weakening (W), by following the method of Jiang (2012) and Jiang & Ramirez (2013). The 24-h intensity change is defined as the difference in V_{max} at the time of the overpass and 24 h in the future. RI was first defined by Kaplan & DeMaria (2003) using the 95th percentile of the cumulative distribution functions of the 24-h intensity change derived from historical best track data. For all TC overpasses used in this study, the 95th percentile of the 24-h intensity change is 30 kt (1 kt = 0.51 m/s). Therefore, RI is defined as the 24-h intensity change >= 30 kt. Table 1 lists the definition of each intensity change category and number of AIRS overpasses over each basin under each intensity change category during 2002–2014. Among these samples, there are 0 RI, 6 SI, 45 N, and 64 W cases that made landfall in the next 24 hours. Fig. 1 shows the geographic distribution of storm centers of the 5019 AIRS overpasses for different intensity change categories. Compared to other intensity change categories, the locations of RI TCs are generally confined within ±20° latitude.

To study the TC warm core, we need to calculate the temperature anomaly first. The temperature anomaly is the difference between the observed temperature in TCs and a reference environmental temperature profile. By following previous studies (Stern & Nolan 2012, Durden 2013, Stern & Zhang 2016, Munsell et al. 2018, Wang & Jiang 2019), in this study the reference profile is calculated for each AIRS TC overpass by taking the average temperature profile within 900–1400 km from the storm center.

3. Results and discussions

3.1. Composite axisymmetric warm-core structure for different intensity change categories

Fig. 2 shows the radial-height composites of azimuthally averaged AIRS retrieved temperature anomalies in TCs for different intensity change categories. All the composites through this study are at the onset stage of different intensity change categories. In general, the height of warm core is located around 300–400 hPa for all TCs. This is consistent with Gao et al. (2017) and Wang & Jiang (2019). The maximum warm-core temperature anomaly is the strongest for TCs in the RI group (~7 K), followed by TCs in the weakening (~6 K), SI (~5 K), and neutral (~4K) group in decreasing order. According to previous studies (Durden 2013; Gao et al. 2017; Wang & Jiang 2019), there is a strong positive correlation between TC intensity and the maximum temperature anomaly. As seen in Table 2, the mean TC intensity V_{max} for weakening storms is the highest (64 kt), followed by RI (57 kt), SI (45 kt), and N (41 kt). Yet the warm-core strength is higher for RI storms than weakening storms, which indicates that not only higher TC intensity but also higher intensification rate is associated with stronger warm-core. In order to isolate the effect of TC size upon intensification from that upon TC general life cycle (i.e. TC intensity), Carrasco et al. (2014) restricted their analysis to only intensifying and steady state storms. A similar perspective can be applied to interpret Fig. 2's result here. By excluding the weakening category, a clear positive relationship between warm-core strength and 24 h future intensification rate can be seen from Fig. 2.

Previous studies have shown the importance of equivalent potential temperature (θ_e) in forecasting TC intensity change (Sikora 1976; Petty & Hobgood 2000). θ_e can be viewed as a measure of convective available potential energy (CAPE) at a particular time. High values of θ_e in the lower atmosphere Sikora 1976

θ_e is calculated using AIRS-retrieved temperature and humidity profiles through a method suggested by Bolton (1980). Much higher θ_e values in the eye of a TC were found by aircraft observations (Hawkins & Imbembo 1976) as well as by numerical calculations (Emanuel 1999). This is consistent with our results in Fig. 2 in which higher θ_e values are located within 30-50 km from the storm center. θ_e is contributed by both temperature and humidity fields. It decreases with height first to the critical level, then increases with height. The critical height near the TC center is about 600 hPa (Fig. 2). Below the critical height, the contribution of humidity to θ_e dominates. The decreasing water vapor amount with height between surface and the critical height causes the θ_e deceasing although the temperature is slightly increasing with height. For RI storms, θ_e below 600 hPa decreases with height at the fastest rate (Fig. 2). Above the critical height, θ_e rapidly increases with height, especially in the eye region, for all TC intensity change categories. However, it increases fastest in RI storms (Fig. 2a), followed by W (Fig. 2d), SI (Fig. 2b), and N storms (Fig. 2c). According to the shear-relative CAPE showed in Fig. 3, it is found that CAPE for RI storms is much higher than other categories. High CAPE and θ_e were found in the eye region in the onset of RI and in the early stage of RI through observations (Sitkowski & Barnes 2009; Barnes & Fuentes 2010) and numerical simulations (Miyamoto & Takemi 2013; Wang & Wang 2014). It was argued that high CAPE in the eye can promote convective activities in the eyewall regions, therefore triggering RI (Wang & Wang 2014).

Among different intensity change categories, RI storms have the highest cloud fraction, which decreases radially from over 0.9 in the inner-core region to around 0.8 at 300 km from the storm center (Fig. 2a). The high cloud fraction in RI storms might be linked with a strengthened convective activity induced by the high CAPE in the inner core area (Wang & Wang 2014). SI storms have the second highest cloud fraction, which decrease radially from over 0.9 in the inner core to a little above 0.7 at 300 km radius (Fig. 2b). For weakening storms, the cloud fraction is around 0.9 in the inner core and decreases to less than 0.7 at 300 km radius (Fig. 2c). Neutral storms have the lowest cloud fraction, which is 0.8 in the inner core (Fig. 2d). When averaging within 500-km from the storm center, the cloud fraction is the highest for RI (0.61), followed by SI (0.58), and N/W (0.53) storms (Table 2). Table 2 also suggests that the TC intensification rate increases with increasing SST and TPW and decreasing environmental vertical wind shear. Wang & Jiang (2019, see their table 5) found that the TC intensity increases with increasing SST and cloud fraction and decreasing shear, but TPW values are similar among different TC intensity stages.

3.2. Composite asymmetric warm-core structure relative to shear

Fig. 4 displays the shear-relative composite temperature anomaly and θ_e averaged vertically from 200 to 600 hPa for four TC intensity change categories. Similar to Fig. 2, the strongest inner-core warm-core strength is seen in RI storms, followed by weakening, SI, and neutral storms in a decreasing order. RI storms also have the highest composite θ_e value (349 K) in the eye, followed by weakening (348 K), SI (347 K), and neutral (345 K) storms. Interestingly, the warm-core structure is asymmetric relative to the environmental vertical wind shear direction in RI storms (Fig. 4a), while it is more symmetric for other intensity change categories (Fig. 4b-d). For RI storms, CAPE showed larger values down-shear quadrant than up-shear quadrant within the radius of 100 km (Fig. 3a, b), which is similar to the results in some previous studies (Molinari & Vollaro 2010; Nguyen et al. 2010; Molinari et al. 2012). CAPE distribution of SI and neutral storms (Fig. 3b, c) are more symmetric than RI storms (Fig. 3a). In weakening cases, the CAPE is larger in up-shear quadrant than in down-shear quadrant (Fig. 3d). However, the differences of CAPE between down-shear and up-shear quadrant in RI storms is much higher than in weakening storms. The high CAPE is favorable to the persistent convection arises in down-shear quadrant in RI storms, which may contribute to the asymmetric warm-core structure showed in Fig. 4a.

3.3. Relationship between warm-core structure and TC intensification rate

To further examine the relationships between the warm-core strength and TC intensity change, Fig. 5 presents scatter plots of the maximum temperature anomaly within the 30 km of the TC center versus 24-h TC intensity change for TCs in all global basins (Fig. 5a) and individual basins (Fig. 5b-f) except for the NIO basin due to the small sample size in this basin (table 3). When considering the whole range of intensity change rate between -80 kt and 80 kt per 24 h, there is clearly a negative correlation between the intensity change rate and warm-core strength, exactly as shown and concluded by Gao et al. (2017). However, a careful scrutiny of Fig. 5 reveals that the negative correlation is mainly driven by the weakening category, same as in Gao et al.'s (2017) Fig. 5a. There are many samples with high initial intensity in the weakening category, especially in Gao et al.'s (2017) study since unlike this study, they included major hurricanes in their sample. Gao et al. (2017) realized the impact of TC intensity and concluded that the negative correlation between the intensity change rate and warm-core strength was mainly driven the negative correlation between TC initial intensity and future intensity change.

As mentioned above, to isolate the effect of a parameter upon TC intensification rate from that upon TC intensity, it is necessary to exclude the weakening category and consider only those samples with intensification rates ≥ 0 as in a few other TC intensification studies (Carrasco et al. 2014; Xu & Wang 2015). As seen in Section 2, weakening cases have the highest percentage of making landfall in the next 24 hours. After excluding the weakening category and part of the samples in the neutral category with intensification rate < 0, the correlation changes from significantly negative with a correlation coefficient $R=-0.29$ to significantly positive with $R=0.23$

for TCs in all basins (Fig. 5a). The positive correlation is the highest in SIO and EPA basins (*R=0.31*), followed by ATL (*R=0.21*), SPA (*R=0.20*), and NWP (*R=0.19*). All correlations in Fig. 5 have a significant level of at least 98% except for the SPA basin due to a small sample size with intensification rates ≥ 0 in this basin (table 3). By excluding weakening cases, Fig. 7 suggests that the warm-core strength is positively correlated with TC intensification rate, which is consistent with previous case studies through observational (Sitkowski & Barnes 2009; Barnes & Fuentes 2010) and numerical (Zhang & Chen 2012; Chen & Zhang 2013; Munsell et al. 2018) methods.

By including both intensifying and weakening samples, Gao et al. (2017) found no significant relationship between TC intensity change and the warm-core height. Fig. 6 here is to re-investigate the relationship. Same as in Wang & Jiang (2019), we calculated a weighted warm-core height by using the definition given by Equation (1) of Ohno et al. (2016). This equation was applied to the temperature anomaly within 30 km of the storm center using the sample in Table 3. Similar as in Gao et al. (2017), no significant correlations are seen between TC intensity change and the weighted warm-core height when looking at the whole intensification rate range including both weakening and intensifying cases (Fig. 6, results in black colors). However, a significant negative correlation is seen between the intensification rate and the pressure level of the weighted warm-core height when considering only those samples with intensification rates ≥ 0 (Fig. 6, results in pink colors). This negative correlation means that the higher the warm-core height is, the larger the TC intensification rate. The correlation coefficients for samples with intensification rates ≥ 0 range between 0.15 and 0.26 for different basins, with the highest correlation in EPA. The significance level of these correlation coefficients is at least 91%. Fig. 6's results are consistent with those numerical simulations showing that higher-level warm core can induce deeper sea level pressure drops therefore greater intensification rates (Zhang & Chen 2012; Chen

& Zhang 2013).

Statistical distributions of the warm-core temperature anomaly and weighted warm-core height within 30 km of the storm center are shown in the box and whisker plots of Fig. 7. The median temperature anomaly and warm-core height increase as the TC intensification rate increases from N to SI to RI. However, the trend is reversed from W to N. As found above in Figs. 5-6, the effect of warm-core strength and height upon the TC intensification is entangled with that upon TC intensity. For the purpose of physical understanding, the effect can be successfully isolated by excluding weakening cases. For the purpose for improving RI prediction, the problem is not that simple since we won't know if the storm is in weakening stage or intensifying stage at the first place. A stronger and/or higher warm-core could be either associated with a stronger storm intensity or higher future intensification rate.

However, it is interesting to see from Fig. 7 that there are different minimum thresholds of the warm-core temperature anomaly and height for different intensity change categories. Statistically RI never happened when the AIRS-derived temperature anomaly within 30 km of the storm center is less than 4 K. It never happened either when the AIRS-derived weighted warm-core height is lower than 450 hPa. These thresholds can be considered as necessary conditions for RI. For other intensity change categories, the minimum thresholds of the temperature anomaly and warm-core height are much lower, therefore they are much easier to satisfy than those for RI. For example, necessary conditions for SI are the temperature anomaly >=1 K and the weighted warm-core height higher than 850 hPa. Similar thresholds as in SI are seen for W and N storms. Therefore, the best suggestion from Fig. 7 for the purpose of improving RI forecasts is the necessary conditions in terms of the minimum threshold of the warm-core temperature anomaly and height.

4. Summary and Conclusions

This study investigates the relationship between the warm-core structure and TC intensity change using 13-year AIRS+AMSU retrieved temperature profiles. The dataset includes 5019 AIRS overpasses in 1061 TCs in global basins during 2002-2014. These overpasses are constrained with storm intensity between tropical storm and category-2 hurricane and under minimal favorable environmental conditions. They are classified into RI, slowly intensifying (SI), neutral (N), and weakening (W) categories based on the difference between 24 h future intensity and the initial intensity at the time of the overpass. The main findings of this study are as follow:

(1) The effect of the warm-core structure upon TC intensification is entangled with that upon TC intensity. It is necessary to exclude the weakening category in order to single out the relationship between TC intensification and warm-core structure from a statistical method.

(2) The composite warm-core temperature anomaly is the strongest in RI storms (~7 K), followed by W (~6 K), SI (~5 K) and N (~ 4K) storms. RI storms also have the highest CAPE in the eye among all intensity change categories. The average cloud fraction, SST, and TPW within 500-km of the storm center are positively correlated with TC intensification rate, while the environmental vertical wind shear is negatively correlated with TC intensification rate.

(3) The warm-core structure of RI storms is asymmetric relative to shear, while it is more symmetric for other intensity change categories. For RI storms, the temperature anomaly and CAPE in the inner core are larger in the down shear quadrant.

(4) When considering only those samples with intensification rates ≥ 0, a significant and positive correlation is found between the warm-core strength and TC intensification rate. The warm-core height is also positively correlated with the TC intensification rate at a high

confidence level. This is against the results of Gao et al. (2017), but consistent with many other observational (Sitkowski & Barnes 2009; Barnes & Fuentes 2010) and numerical (Zhang & Chen 2012; Chen & Zhang 2013; Munsell et al. 2018) studies.

(5) Different from other intensity change categories including the weakening group, the necessary conditions for RI are: a) the AIRS-derived temperature anomaly within 30 km of the storm center must be greater than 4 K, and b) the AIRS-derived weighted warm-core height must be higher than 450 hPa. This is the most important finding of this study, which can shed light on improving the practical RI forecasts.

Acknowledgements

This work was jointly supported by the National Natural Science Foundation of China (Grant 41875070, 41365005) and the Hainan Key Cooperation Program (Grant ZDYF2019213). This work was conducted during the first author's 1-yr visit at FIU under the supervision of the second author. The authors really appreciate the constructive comments from two anonymous reviewers that contribute greatly in improving the manuscript. AIRS data (AIRXRET Version 6) are downloaded from the NASA Goddard Earth Science Data and Information Services Center and TC best-track data are provided by the JTWC and NHC through their websites (https://www.nhc.noaa.gov/data). The authors are grateful to Drs. Cheng Tao and Yongxian Pei for their assistance in AIRS data processing.

REFERENCES

Alvey, G., III, Zawislak, J., & Zipser, E. (2015). Precipitation Properties Observed during Tropical Cyclone Intensity Change. *Mon. Wea. Rev.*, **143,** 4476–4492. https://doi.org/10.1175/MWR-D-15-0065.1.

Aumann, H. H., & Coauthors, (2003). AIRS/AMSU/ HSB on the Aqua mission: Design, science objectives, data products, and processing systems. *IEEE Trans. Geosci. Remote Sens.*, **41**, 253–264.

Barnes, G. M., & Fuentes, P. (2010). Eye excess energy and the rapid intensification of Hurricane Lili (2002). *Mon. Wea. Rev*., **138**, 1446–1458.

Bolton, D., (1980). The computation of equivalent potential temperature. *Mon. Wea. Rev*., **108**, 1046–1053.

Carrasco, C. A., Landsea, C. W., & Lin, Y. (2014). The influence of tropical cyclone size on its intensification. Weather Forecasting, 29, 582–590. https://doi.org/10.1175/WAF-D-13-00092.1.

Cecil, D. J., Zipser, E. J. (1999). Relationships between tropical cyclone intensity and satellite-based indicators of inner core convection: 85-GHz ice-scattering signature and lightning. *Mon. Weather Rev*. **127**, 103–123.

Chahine, M.T., & Coauthors. (2001). AIRS level 2 unified retrieval for core products ATBD. [Available online at http://eospso.gsfc.nasa.gov/eos_homepage/ for_scientists/atbd.]

Chahine, M.T., & Coauthours. (2006). AIRS: improving weather forecasting and providing new data on greenhouse gases. *Bull. Am. Meteorol. Soc.*, **87(7)**, 911–926.

Chen, H., & Zhang, D. L. (2013). On the rapid intensification of Hurricane Wilma (2005). Part II: Convective bursts and the upper-level warm core. *J. Atmos. Sci*. **70**, 146–162. https://doi.org/10.1175/JAS-D-12-062.1.

Dee, D. P., & authors. (2011). The ERA-Interim reanalysis: configuration and performance of the data assimilation system. *Q. J. Roy. Meteor. Soc.* **137**, 553–597.

DeMaria, M., Sampson, C. R., Knaff, J. A., & Musgrave, K. D. (2014). Is tropical cyclone intensity guidance improving? *Bull. Amer. Meteor. Soc*. **95**, 387–398.

Durden, S. L. (2013). Observed tropical cyclone eye thermal anomaly profiles extending above 300 hPa. *Mon. Weather Rev*. **141**, 4256–4268.

Emanuel, K. (1999). Thermodynamic control of hurricane intensity. *Nature*, **401**, 665–669.

Fischer, M.S., Tang, B. H. Corbosiero, K. L., & Rozoff, C. M. (2018). Normalized Convective Characteristics of Tropical Cyclone Rapid Intensification Events in the North Atlantic and Eastern North Pacific. *Mon. Wea. Rev.*, **146,** 1133–1155.

Gao, S., Chen, B. C., Li, T., Wu, N., & Deng, W. (2017). AIRS-observed warm core structures of tropical cyclones over the western North Pacific. Dynamics of Atmospheres and Oceans, **77**, 100–106.

Hawkins, H. F., & Imbembo, S. M. (1976). The structure of a small, intense hurricane-Inez 1966. *Mon. Wea. Rev*., **104**, 418–442.

Hendricks, E. A., Montgomery, M. T., & Davis, C. A. (2004). The role of ‘‘vortical’’ hot towers in the formation of Tropical Cyclone Diana (1984). *J. Atmos. Sci*. **61**, 1209–1232.

Hendricks, E. A., Peng, M. S., Fu, B. & Li, T. (2010). Quantifying environmental control on tropical cyclone intensity change. *Mon. Wea. Rev*., **138**, 3243–3271. doi:10.1175/2010MWR3185.1.

Hirschberg, P. A., & Fritsch, J. M. (1993). On understanding height tendency. *Mon. Wea. Rev*. **121(9)**, 2646–2661.

Houze, R. A., Jr., Lee, W., & Bell, M. M. (2009). Convective con- tribution to the genesis of Hurricane Ophelia (2005). *Mon. Wea Rev*. **137**, 2778–2800.

Jiang, H. (2012). The relationship between tropical cyclone intensity change and the strength of inner-core convection. *Mon. Wea Rew*. **140**, 1164–1176.

Jiang, H., & Ramirez, E. M. (2013). Necessary conditions for tropical cyclone rapid intensification as derived from 11 years of TRMM data. *J. Clim*. **26**, 6459–6470.

Jiang, H., Zagrodnik, J. P., Tao, C., & Zipser, E. J. (2018). Classifying precipitation types in tropical cyclones using the NRL 37 GHz color product. *J. Geophys. Res.*, **123**, 5509–5524. https://doi.org/10.1029/2018JD028324.

Kaplan, J., & DeMaria, M. (2003). Large-scale characteristics of rapidly intensifying tropical cyclones in the North At- lantic basin. *Weather Forecasting*, **18**, 1093–1108.

Kaplan, J., DeMaria, M., & Knaff, J. A. (2010). A revised tropical cyclone rapid intensification index for the Atlantic and eastern North Pacific basins, *Weather Forecasting*, **25**, 220–241.

Kelley, O. A., Stout, J., & Halverson, J. B. (2004). Tall precipitation cells in tropical cyclone eyewalls are associated with tropical cyclone intensification. *Geophys. Res. Lett*. **31**, L24112.

Kelley, O. A., Stout, J., & Halverson, J. B. (2005). Hurricane intensification detected by continuously monitoring tall precipitation in the eyewall. *Geophys. Res. Lett*. **32**, L20819.

Kieper, M., & Jiang, H. (2012). Predicting tropical cyclone rapid intensification using the 37 GHz ring pattern identified from passive microwave measurements. *Geophys. Res. Lett.*, **39**, L13804, doi:10.1029/2012GL052115.

Kieu, C., Tallapragada, V., & Hogsett, W. (2014). Vertical structure of tropical cyclones at onset of the rapid intensification in the HWRF model. *Geophys. Res. Lett*. **41(9)**, 3298–3306.

Knaff, J. A., Seseske, S. A., DeMaria, M., & Demuth, J. L. (2004). On the influences of vertical wind shear on symmetric tropical cyclone structure derived from AMSU. *Mon. Wea. Rev*., **132**, 2503–2510.

Lin, J., & Qian, T. (2019), Rapid Intensification of tropical cyclones observed by AMSU satellites. Geophysical Research Letter, 46, 7054-7062.

Merrill, R. T. (1988). Environmental influences on hurricane intensification. *J. Atmos. Sci*. **45**, 1678–1687.

Molinari, J., Romps, D. M., Vollaro, D., & Nguyen L. (2012), CAPE in tropical cyclones, *J. Atmos. Sci*., **69**, 2452–2463, doi:10.1175/JAS-D-11- 0254.1.

Molinari, J., & Vollaro, D. (2010). Rapid intensification of a sheared tropical storm. *Mon. Wea. Rev*., 138, 3869–3885.

Miyamoto, Y., & Takemi, T. (2013). A transition mechanism for the spontaneous axisymmetric intensification of tropical cyclones. *J. Atmos. Sci*., **70**, 112–129.

Montgomery, M. T., Nicholls, M. E., Cram, T. A., & Saunders, A. B. (2006). A vortical hot tower route to tropical cyclogenesis. *J. Atmos. Sci*. **63**, 355–386.

Moustafa, T. C., & Coauthors. (2006). AIRS: Improving weather forecasting and providing new data on greenhouse gases. *Bull. Amer. Meteor. Soc*., 911–926. *https://doi.org/10.1175/BAMS-87-7-911*.

Munsell, E. B., Zhang, F., Braun, S., & Didlake, A. C. (2018). The Inner-core temperature structure of Hurricane Edouard (2014) observations and Ensemble variability. *Mon. Weather Rev.*, **146**, 135–155. DOI: 10.1175/MWR-D-17-0095.1.

Nguyen, L., Thomas, D., Vollaro, D., & Molinari, J. (2010). Thermodynamic structure of tropical cyclones from dropsondes. Extended Abstracts, *29th Conf. on Hurricanes and Tropical Meteorology*, Tucson, AZ, Amer. Meteor. Soc., P2.42.

Nolan, D. S., & Grasso, L. D. (2003). Nonhydrostatic, three- dimensional perturbations to balanced, hurricane-like vortices. Part II: Symmetric response and nonlinear simulations. *J. Atmos. Sci.* **60**, 2717–2745.

Nolan, D. S, Moon, Y., & Stern, D. P. (2007). Tropical cyclone intensification from asymmetric convection: Energetics and efficiency. *J. Atmos. Sci*. **64**, 3377–3405.

Ohno, T., & Satoh, M. (2015). On the warm core of a tropical cyclone formed near the tropopause. *J. Atmos. Sci*. **72**, 551–571, https://doi.org/10.1175/JAS-D-14-0078.1.

Ohno, T., Satoh, M., & Yamada, Y. (2016). Warm Cores, Eyewall Slopes, and Intensities of Tropical Cyclones Simulated by a 7-km-Mesh Global Nonhydrostatic Model. *J. Atmos Sci.*, **73**, 4289–4309.

Petty, K. R., & Hobgood, J. S. (2000). Improving Tropical Cyclone Intensity Guidance in the Eastern North Pacific. *Weather Forecasting*, **15**, 233–244.

Shimada, U., Aonashi, K., & Miyamoto, Y. (2017). Tropical cyclone intensity change and axisymmetricity deduced from GSMaP. *Mon. Wea. Rev.*, **145**, 1003–1017, doi:10.1175/MWR-D-16-0244.1.

Shu, S., Ming, J., & Chi, P. (2012). Large-scale characteristics and probability of Rapidly intensifying tropical cyclones in the western north pacific basin. *Weather Forecasting*, **27**, 411–423. https://doi.org/10.1175/WAF-D-11-00042.1.

Sikora, C. R. (1976). An investigation of equivalent potential temperature as a measure of tropical cyclone intensity. FLEWEACEN Tech. Note JTWC 76–312 pp. [Available from U.S. Naval Oceanography Command Center/Joint Typhoon Warning Center, FPO, San Francisco, CA 96630.]

Sitkowski, M., & Barnes, G. M. (2009). Low-level thermodynamic, kinematic, and reflectivety fields of hurricane Guillermo (1997) during rapid intensification. *Mon. Wea. Rev.*, **137**, 645-663. https://doi.org/10.1175/2008MWR2531.1.

Stern, D. P., & Nolan, D. S. (2012). On the height of the warm core in tropical cyclones. *J. Atmos. Sci*., **69(5)**, 1657–1680.

Stern, D. P., Vigh, J. L., Nolan, D. S., & Zhang, F. (2015). Revisiting the relationship between eyewall contraction and intensification. *J. Atmos. Sci*., **72**, 1283–1306.

Stern, D. P., & Zhang, F. (2013). How Does the Eye Warm? Part I: A potential temperature budget analysis of an idealized tropical cyclone. *J. Atmos. Sci.* **70**, 73–90.

Stern, D. P., & Zhang F. (2016). The warm-core structure of Hurricane Earl (2010). *J. Atmos. Sci.*, **73**, 3305–3328. https://doi.org/10.1175/ JAS-D-15-0328.1.

Susskind, J., Barnet, C., & Blaisdell, J. (2003). Retrieval of atmospheric and surface parameters from AIRS/ AMSU/HSB data in the presence of clouds. *IEEE Trans. Geosci. Remote Sens.*, **41**, 390-409.

Tao, C., & Jiang, H. (2015). Distributions of shallow to very deep Precipitation–Convection in rapidly intensifying tropical cyclones. *J. Climate*, **28**, 8791–8824.

Tao, C., Jiang, H., & Zawislak, J. (2017). The Relative Importance of Stratiform and Convective Rainfall in Rapidly Intensifying Tropical Cyclones, *Mon. Wea. Rev*., **145**, 795–809.

Wang, X. & Jiang, H. (2019). A 13-Year Global Climatology of Tropical-Cyclone Warm-Core Structures from AIRS Data. *Mon. Wea. Rev*.,**147**, 773–790.

Wang, Y., & Wu, C. C. (2004). Current understanding of tropical cyclone structure and intensity changes-A review. *Meteor. Atmos. Phys*. **87**, 257–278.

Wang, Y., & Wang, H. (2014). A Numerical Study of Typhoon Megi (2010). Part I: Rapid Intensification. *Mon. Wea. Rev*., **142**, 29–48

Xu, J., & Wang, Y. (2015). A statistical analysis on the dependence of tropical cyclone intensification rate on the storm intensity and size in the North Atlantic. *Weather Forecasting,* 30, 692–701. https://doi.org/10.1175/WAF-D-14-00141.1.

Xu, W., Rutledge, S. A., Zhang W., 2017. Relationships between total lightning, deep convection, and tropical cyclone intensity change. J. Geophys. Res. Atmos. **122**, 7047–7063.

Zagrodnik, J., & Jiang, H. (2014). Rainfall, Convection, and Latent Heating Distributions in Rapidly Intensifying Tropical Cyclones. *J. Atmos. Sci.*, **71**, 2789–2809.

Zawislak, J., Jiang, H., Alvey III, G. R., Zipser, E. J., Rogers, R. F., Zhang, J., & Stevenson, S. (2016). Observations of the structure and evolution of Hurricane Edouard (2014) during intensity change. Part I: Relationship between the thermodynamic structure and precipitation. *Mon. Wea. Rev*., **144**, 3333–3354.

Zhang, D. L., & Chen, H. (2012). Importance of the upper-level warm core in the rapid intensification of a tropical cyclones. *Geophys. Res. Lett*. **39(2)**, L02806.

Figure Captions:

Fig. 1: The geographic distribution of storm center covered by the 5019 selected AIRS overpasses during 2002-1014. Colors represent different intensity change categories.

Fig. 2: Radial-height composites of azimuthally averaged AIRS-retrieved temperature anomaly (K, color-shaded) and equivalent potential temperatures (K, grey contour) for different intensity change categories: (a) RI, (b) SI, (c) N, and (d) W. The white curve indicates cloud fraction.

Fig. 3: The shear-relative temperature anomaly (K, color-shaded) and equivalent potential temperature (K, contour) averaged vertically from 200 to 600 hPa for different intensity change categories: (a) RI, (b) SI, (c) N, and (d) W. The shear vector is pointing to the right side of each panel.

Fig. 4: The shear-relative CAPE (J kg^{-1}) for different intensity change categories: (a) RI, (b) SI, (c) N, and (d) W. The shear vector is pointing to the right side of each panel. The shear vector is pointing to the right side of each panel.

Fig. 5: Scatter plots of the maximum temperature anomaly (TA, K) within the 30 km of the TC center versus 24-h TC intensity change (kt) for TCs in (a) all basins, (b) ATL, (c) EPA, (d)

NWP, (e) SIO, and (f) SPA basins. Dots in different colors represent different intensity change categories. Correlation coefficients, P values of the statistical significance, and linear regression fitting lines for all samples (with both positive and negative intensification rates) are shown in black, and for samples with intensification rates ≥ 0 are in pink.

Fig. 6: Same as Fig. 5 but for the weighted height (hPa) of maximum temperature anomaly within the 30 km of the TC center versus 24-h TC intensity change (kt).

Fig. 7: Box and whisker plots of (a) the maximum temperature anomaly (TA, K) and (b) the weighted height (hPa) of maximum temperature anomaly within the 30 km of the TC center for different intensity change categories. The top of the box represents the 75% percentile, the center line the median, and the bottom of the box the 25% percentile. The whiskers extend to minimum and maximum of the range and outliers are plotted individually with circles.

Table 1: The number of AIRS overpasses for each intensity change category over each basin during 2002-2014.

Category	Definition (kt)	ATL	EPA	NWP	NIO	SIO	SPA	Total
RI		59	65	182	14	87	57	464
SI		228	186	549	64	346	137	1510
N		321	440	602	137	617	176	2293
W		79	208	213	33	168	51	752
Total		687	899	1546	248	1218	421	5019

Table 2: Mean values of V_{max}, environmental vertical wind shear, SST, cloud fraction, TPW, and CAPE for different TC intensity change categories.

Category	Vmax (kt)	Shear (ms^{-1})	SST (^{o}C)	Cloud fraction (%)	TPW (mm)	CAPE ($J\ Kg^{-1}$)
RI	57	5.59	28.66	61	52	2084
SI	45	6.51	28.43	58	52	1677
N	41	8.02	27.64	53	50	1521
W	64	8.23	26.91	53	49	1804

Table 3: Number of AIRS profiles within 30 km of the storm center over each basin for each TC intensity change category.

Basin	RI	SI	N	W	Total
ATL	9	73	170	43	323
EPA	7	25	196	85	281

NWP	27	139	253	141	545
NIO	1	18	52	10	59
SIO	10	70	281	77	321
SPA	3	18	67	30	118
Total	57	343	1019	386	1804

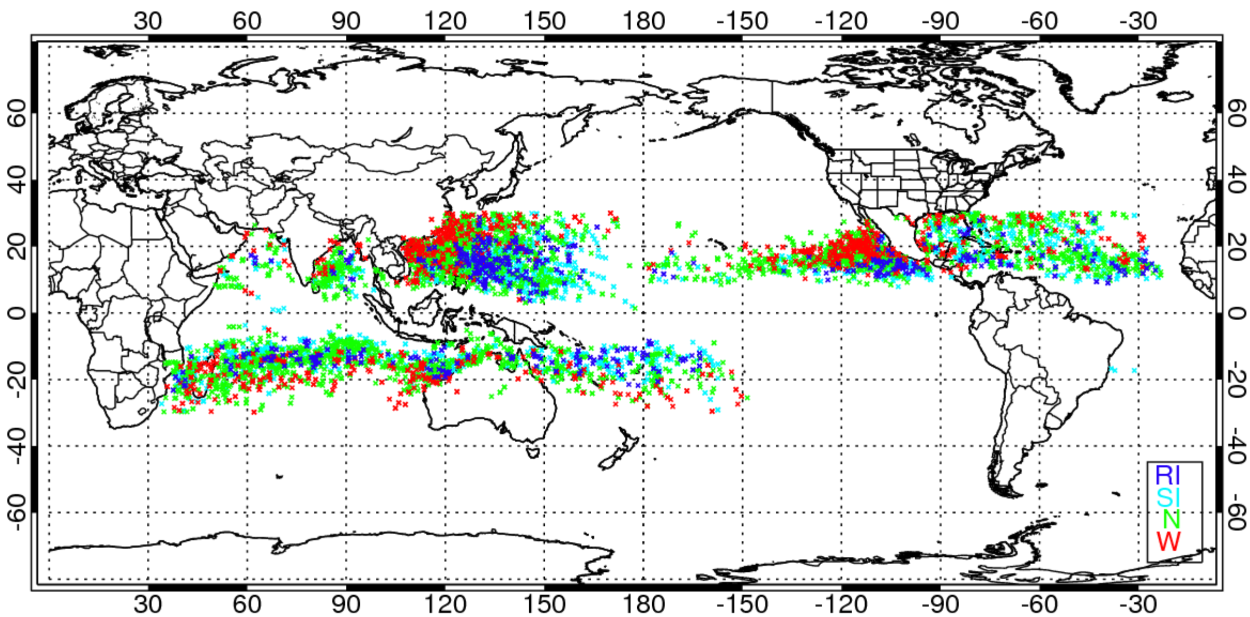

Fig. 1: The geographic distribution of storm center covered by the 5019 selected AIRS overpasses during 2002-2014. Colors represent different intensity change categories.

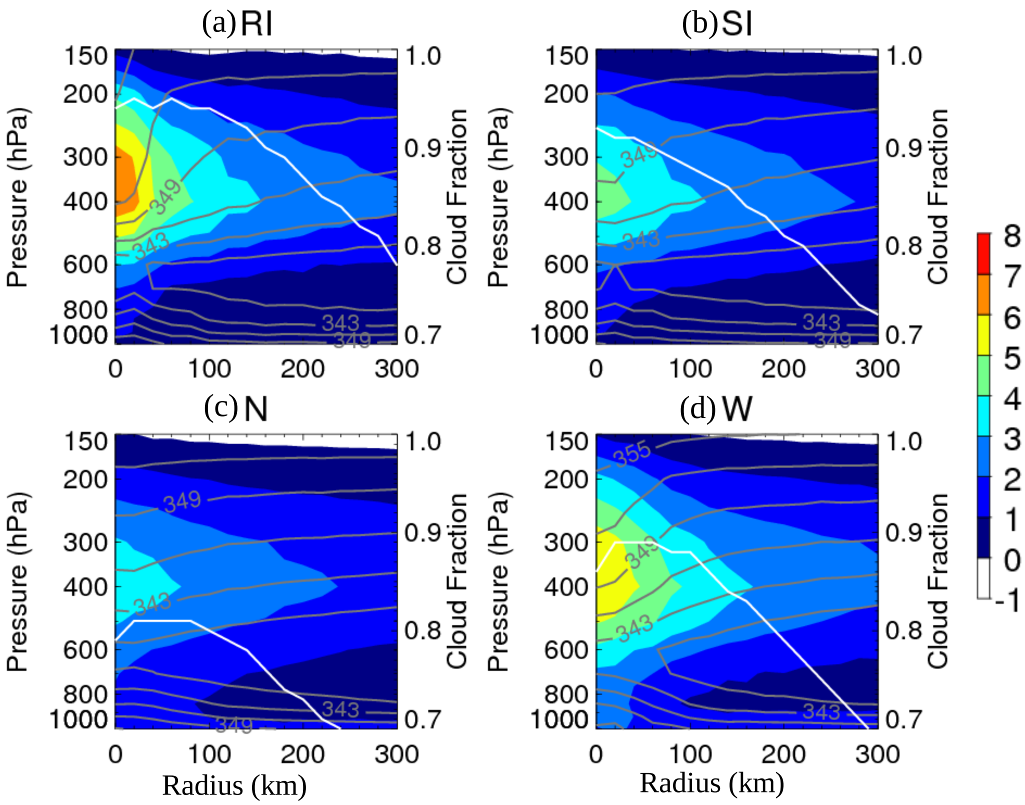

Fig. 2: Radial-height composites of azimuthally averaged AIRS-retrieved temperature anomaly (K, color-shaded) and equivalent potential temperatures (K, grey contour) for different intensity change categories: (a) RI, (b) SI, (c) N, and (d) W. The white curve indicates cloud fraction.

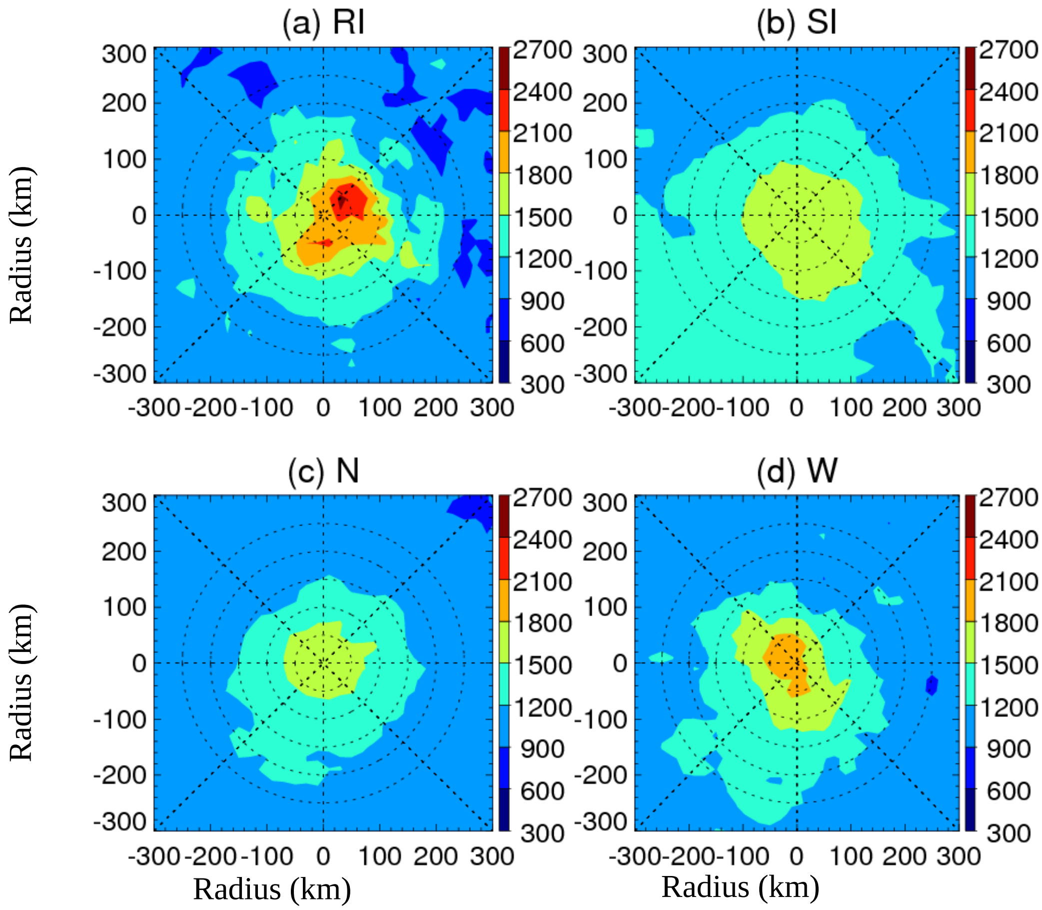

Fig. 3: The shear-relative CAPE (J kg^{-1}) for different intensity change categories: (a) RI, (b) SI, (c) N, and (d) W. The shear vector is pointing to the right side of each panel. The shear vector is pointing to the right side of each panel.

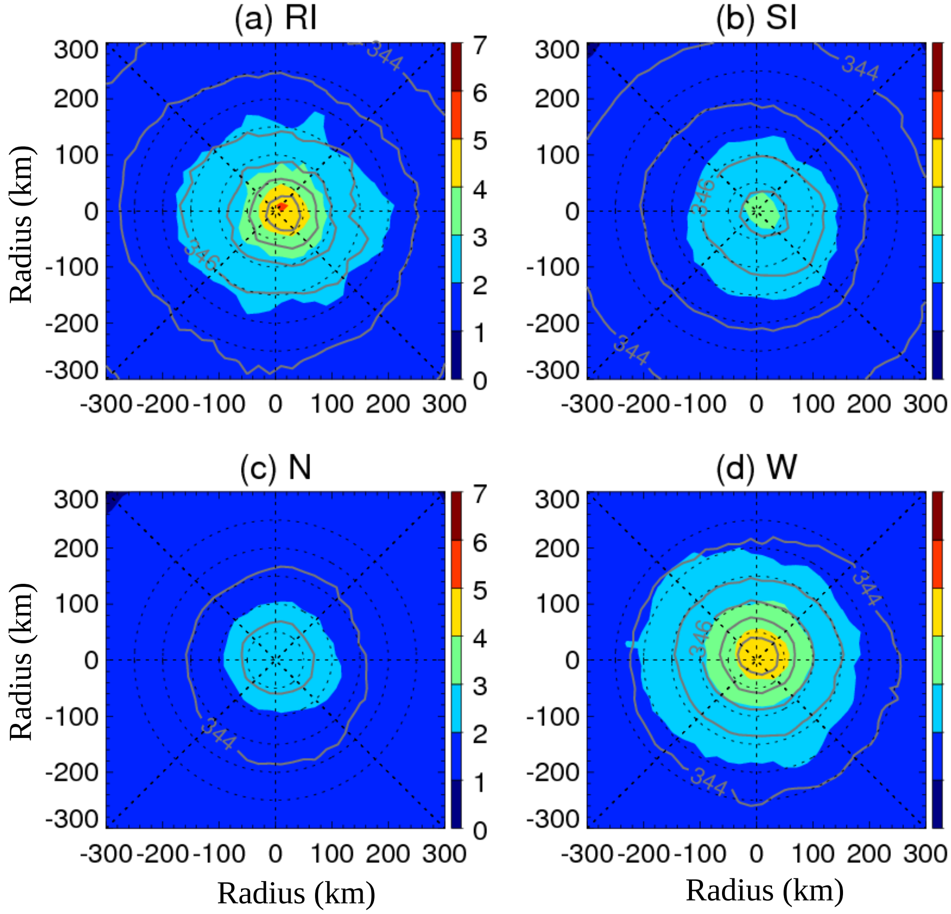

Fig. 4: The shear-relative temperature anomaly (K, color-shaded) and equivalent potential temperature (K, contour) averaged vertically from 200 to 600 hPa for different intensity change categories: (a) RI, (b) SI, (c) N, and (d) W. The shear vector is pointing to the right side of each panel.

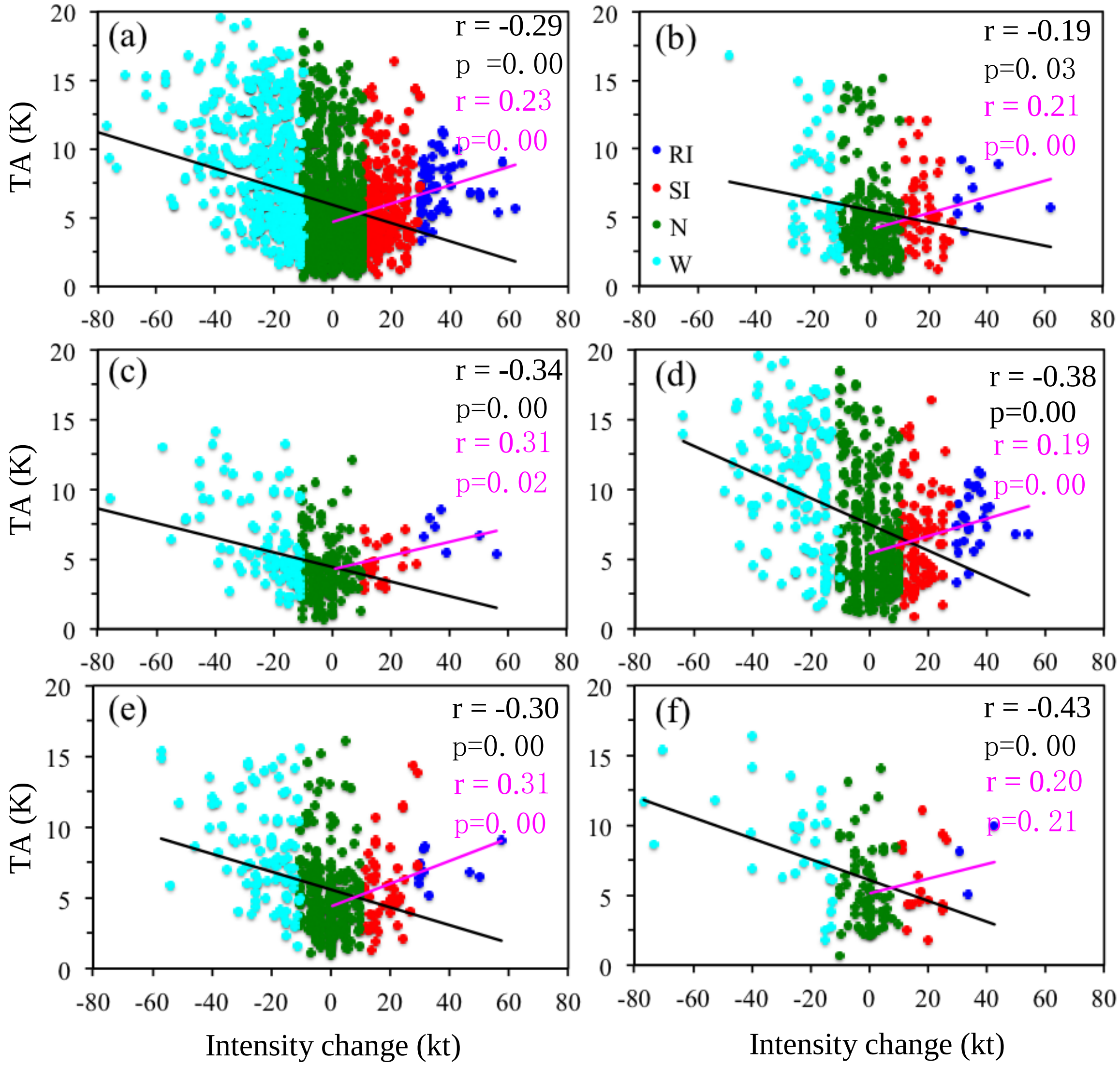

Fig. 5: Scatter plots of the maximum temperature anomaly (TA, K) within the 30 km of the TC center versus 24-h TC intensity change (kt) for TCs in (a) all basins, (b) ATL, (c) EPA, (d) NWP, (e) SIO, and (f) SPA basins. Dots in different colors represent different intensity change categories. Correlation coefficients, P values of the statistical significance, and linear regression fitting lines for all samples (with both positive and negative intensification rates) are shown in black, and for samples with intensification rates ≥ 0 are in pink.

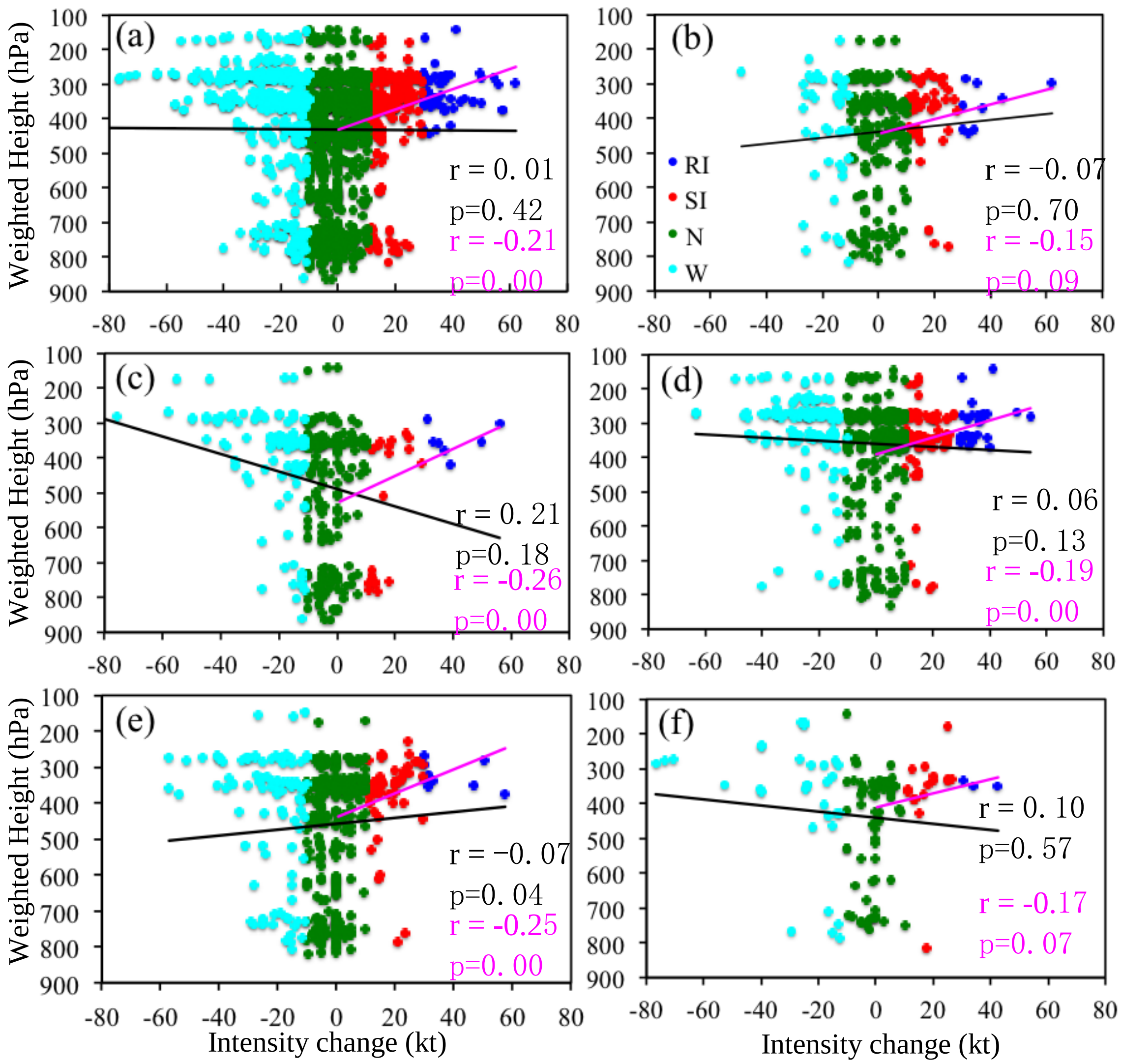

Fig. 6: Same as Fig. 5 but for the weighted height (hPa) of maximum temperature anomaly within the 30 km of the TC center versus 24-h TC intensity change (kt).

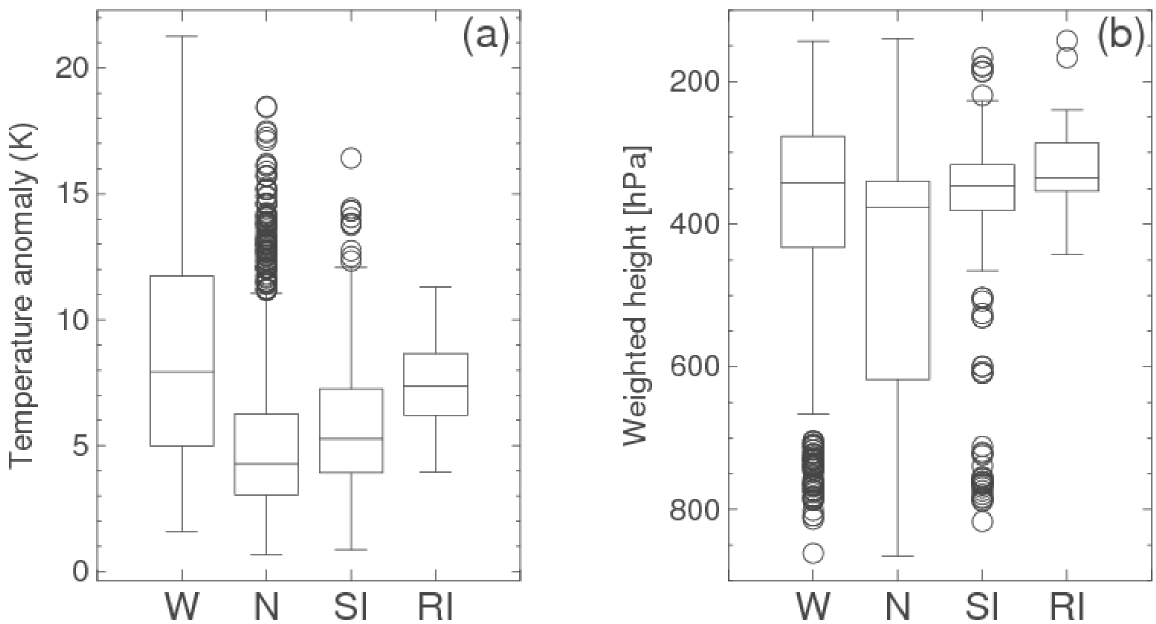

Fig. 7: Box and whisker plots of (a) the maximum temperature anomaly (TA, K) and (b) the weighted height (hPa) of maximum temperature anomaly within the 30 km of the TC center for different intensity change categories. The top of the box represents the 75% percentile, the center line the median, and the bottom of the box the 25% percentile. The whiskers extend to minimum and maximum of the range and outliers are plotted individually with circles.